Impact of the Transition Metal Dopant in Zinc Oxide Lithium-Ion Anodes on the Solid Electrolyte Interphase Formation

Tobias Eisenmann, Jakob Asenbauer, Seyed Javad Rezvani, Thomas Diemant,
Rolf Jürgen Behm, Dorin Geiger, Ute Kaiser, Stefano Passerini, and Dominic Bresser*

Conversion/alloying materials (CAMs) provide substantially higher specific capacities than graphite, the state-of-the-art lithium-ion battery anode material. The ability to host much more lithium per unit weight and volume is, however, accompanied by significant volume changes, which challenges the realization of a stable solid electrolyte interphase (SEI). Herein, the comprehensive characterization of the composition and evolution of the SEI on transition metal (TM) doped zinc oxide as CAM model compound, is reported, with a particular focus on the impact of the TM dopant (Fe or Co). The results unveil that the presence of iron specifically triggers the electrolyte decomposition. However, this detrimental effect can be avoided by stabilizing the interface with the electrolyte by a carbonaceous coating. These findings provide a great leap forward toward the enhanced understanding of such doped materials and (transition) metal oxide active materials in general.

T. Eisenmann, Dr. J. Asenbauer, Dr. T. Diemant, Prof. R. J. Behm,
Prof. S. Passerini, Dr. D. Bresser
Helmholtz Institute Ulm (HIU)
Helmholtzstrasse 11, Ulm 89081, Germany
E-mail: dominic.bresser@kit.edu
T. Eisenmann, Dr. J. Asenbauer, Prof. S. Passerini, Dr. D. Bresser
Karlsruhe Institute of Technology (KIT)
P.O. Box 3640, Karlsruhe 76021, Germany
Dr. S. J. Rezvani
INFN, Laboratori Nazionali di Frascati
Via Enrico Fermi 54, Frascati 00044, Italy
Dr. S. J. Rezvani
Consiglio Nazionale delle Ricerche (CNR)
IOM-CNR, Laboratorio TASC
Basovizza SS-14, km 163.5, Trieste 34149, Italy
Dr. T. Diemant, Prof. R. J. Behm
Institute of Surface Chemistry and Catalysis
Ulm University
Albert-Einstein-Allee 47, Ulm 89081, Germany
Dr. D. Geiger, Prof. U. Kaiser
Central Facility for Electron Microscopy
Ulm University
Albert-Einstein-Allee 11, Ulm 89081, Germany

1. Introduction

Lithium-ion batteries (LIBs) are nowadays the power source of choice for portable electronics and electric vehicles.[1,2] One major reason for the success of LIBs is the successful introduction of graphite with a specific capacity of 372 mAh g^{-1} as active material for the negative electrode, thanks to the identification of ethylene carbonate (EC) and vinylene carbonate as providers of suitable building blocks for the formation of a long-term stable solid electrolyte interphase (SEI).[3,4] The SEI on graphite electrodes has been thoroughly investigated in the last two decades, finding that, typically, inorganic compounds such as LiF, Li$_2$CO$_3$, and Li$_2$O form a dense inner layer with an organic and flexible outer layer.[5–8] The further improvement of LIBs in terms of energy and power density, however, requires the development of new active materials, which can host more lithium per unit weight and volume while providing substantially faster charging rates. On the anode side, research efforts focus on the development of active materials storing lithium cations via mechanisms alternative to ion insertion. Conversion and alloying materials, for instance, offer substantially higher specific capacities and frequently shorter dis-/charging times than graphite. Nevertheless, they face several intrinsic challenges, including an extensive volume variation, which may lead to particle fracturing and pulverization. The potential advantages and remaining challenges of alloying and conversion materials were summarized in various excellent review articles.[9–16] In an attempt to overcome these challenges, it has been proposed to combine both mechanisms in a single type of material, namely, conversion/alloying materials (CAMs).[17] Carbon-coated ZnTM$_2$O$_4$ (TM = transition metal = Co, Mn, Fe), for instance, offers high specific capacities (around 1000 mAh g^{-1}) at lower de-/lithiation potentials than the corresponding conversion-type transition metal oxides.[17] Nonetheless, just like pure conversion-type compounds, these materials commonly exhibit a continuous increase in capacity upon long-term cycling.[18–20] This has been assigned to the detrimental "quasi-reversible" SEI formation, causing continuous electrolyte decomposition,[16,19,21–25] thus highlighting the need for a stabilized interface with the electrolyte. Besides, a general shortcoming of these spinel ZnTM$_2$O$_4$ compounds is the rather high relative contribution of the conversion reaction to the overall capacity, resulting in a rather high average

de-/lithiation potential. TM-doped ZnO, also acting as CAM, provides a substantially higher fraction of the alloying reaction, which enables higher energy densities at the full-cell level.[26,27] $Zn_{0.9}Co_{0.1}O$ provides a stable reversible specific capacity of about 1000 mAh g^{-1}, comparable to $ZnCo_2O_4$, however, accompanied by a lower average de-/lithiation potential.[26,28,29] Remarkably, TM-doped zinc oxides are generally less prone to the continuous rise in capacity upon long-term cycling, although the choice of the TM dopant plays a decisive role for the cycling stability. As a matter of fact, $Zn_{0.9}Fe_{0.1}O$ shows less stable cycling without applying a carbon coating[26] while the overall electrochemical reactions, at least those occurring in the bulk material, appear to be very similar.[28,30–32] These findings suggest that in general, the elemental composition of CAMs is pivotal for the reactions occurring at the electrode|electrolyte interface, which eventually determine the electrochemical performance.

To elucidate the impact of the elemental composition on the electrolyte decomposition and SEI formation, we provide herein, a comprehensive comparison of the surface film formation and its evolution upon cycling for a series of CAMs, that is, ZnO, $Zn_{0.9}Co_{0.1}O$, $Zn_{0.9}Fe_{0.1}O$, and carbon-coated $Zn_{0.9}Fe_{0.1}O$. By employing ex situ X-ray photoelectron spectroscopy (XPS) and ex situ soft X-ray absorption spectroscopy (XAS), in both total electron yield (TEY) and total fluorescence yield (TFY) mode, this complementary study allows for analyzing the SEI on such materials at different information depths (ID), thus, providing valuable insights about its thickness and depth-dependent composition.

2. Results and Discussion

2.1. Basic Physicochemical Characterization

ZnO, $Zn_{0.9}Co_{0.1}O$, $Zn_{0.9}Fe_{0.1}O$, and $Zn_{0.9}Fe_{0.1}O$–C nanoparticles were synthesized via an environmentally benign and easy one-pot synthesis based on metal-gluconate precursors and sucrose, as described by Bresser et. al.[26] The corresponding X-ray diffraction (XRD) patterns (Figure S1, Supporting Information) do not show any phase impurities for any of the samples, indicating a successful introduction of the transition metals (TM) into the wurtzite lattice in the case of $Zn_{0.9}Co_{0.1}O$, $Zn_{0.9}Fe_{0.1}O$, and $Zn_{0.9}Fe_{0.1}O$–C. In fact, a detailed structural analysis of these materials revealed that the TM cations are replacing the zinc cations in the oxygen tetrahedra, accompanied by a slight variation of the lattice parameters.[33] The crystallinity and/or crystallite size decreases in the order ZnO > $Zn_{0.9}Co_{0.1}O$ > $Zn_{0.9}Fe_{0.1}O$ as a result of the different transition metal doping. The additional thermal treatment in the case of $Zn_{0.9}Fe_{0.1}O$–C leads to a greater crystallinity and/or a slightly larger crystallite size compared to $Zn_{0.9}Fe_{0.1}O$. Scanning electron microscopy (SEM) micrographs for all samples are presented in Figure S2, Supporting Information, revealing that the nanoparticle size decreases in the same order (i.e., ZnO > $Zn_{0.9}Co_{0.1}O$ > $Zn_{0.9}Fe_{0.1}O$–C ≈ $Zn_{0.9}Fe_{0.1}O$). This is in good agreement with the transmission electron microscopy (TEM) micrographs of $Zn_{0.9}Co_{0.1}O$ and $Zn_{0.9}Fe_{0.1}O$ (Figure S3, Supporting Information) as well as with results of previous studies.[26,28,30,32,33] The carbon content in $Zn_{0.9}Fe_{0.1}O$–C has been determined via thermogravimetric analysis (TGA)

to be around 10% (Figure S4, Supporting Information) and the homogeneous coverage of the $Zn_{0.9}Fe_{0.1}O$ particles has been confirmed by TEM and energy-dispersive X-ray spectroscopy (EDX; Figure S5, Supporting Information).

### 2.2. Soft XAS Analysis – Pristine Electrodes

Soft XAS measurements on the pristine electrodes were performed in order to qualitatively confirm the absence of phase impurities and, thus, the successful substitution of Zn with Fe and Co, while simultaneously serving as reference data for the investigation of the SEI. Spectra were collected at the Zn L-edges, TM L-edges, and O K-edge in both TEY and TFY mode (**Figure 1**). The Zn L-edge TEY spectra of all four samples in Figure 1a show the typical spectral features and oscillations expected for the local Zn environment in wurtzite ZnO,[30] without any additional features from other phases such as, for example, spinel phases, which show a significantly different fine structure above the L$_3$ edge.[34,35] The intensity of the spectrum for $Zn_{0.9}Fe_{0.1}O$–C in TEY is substantially lower compared to the others due to the carbon coating. The fluorescence spectra, however, show rather comparable intensities (Figure 1b). This nicely demonstrates the different IDs of the two complementary modes. The TM L-edge TEY spectra in Figure 1c reveal that iron is mostly trivalent in $Zn_{0.9}Fe_{0.1}O$, while cobalt is divalent. Furthermore, the ratio of Fe(III):Fe(II) decreases slightly upon application of the carbon coating, indicating that iron is partially reduced (presumably at the particle surface). This is in good agreement with previous findings, which revealed a ratio of 5% divalent iron in such case.[33] The fluorescence spectra in Figure 1d show essentially the same local and electronic structure, confirming the homogeneity of the sample composition within the different IDs. The O K-edge spectra in Figure 1e,f also show the typical spectral features A, B, C, and D of wurtzite ZnO, which arise from O 1s to empty O 2p orbital transitions.[36] The iron containing samples also develop a small shoulder related to the Fe(III)-O coordination at around 530 eV.[25]

In summary, the soft XAS characterization of pristine electrodes qualitatively shows that ZnO was successfully doped with iron (III) and cobalt (II), in agreement with a detailed structural analysis reported earlier.[33] The combination of TEY and TFY, furthermore, shows that the chemical and electronic structure of Zn, Fe, and Co do not change with the different ID, indicating a homogeneous composition in the extended surface region.

2.3. Electrochemical Characterization

The results of the comparative electrochemical analysis, serving also as basis for the selection of appropriate ex situ samples for the following XAS and XPS experiments, are shown in **Figure 2**.

The first cycle dis-/charge profiles of all four samples (Figure 2a) demonstrate the differences upon initial lithiation and delithiation of the (TM-doped) ZnO. Pure ZnO shows only a short plateau at around 0.75 V, most likely due to SEI formation, followed by a long potential plateau corresponding to the conversion reaction (i.e., the reduction of ZnO to Li_2O and Zn^0) and a subsequent sloping region related to the alloying reaction

ADVANCED
SCIENCE NEWS
www.advancedsciencenews.com

small
methods
www.small-methods.com
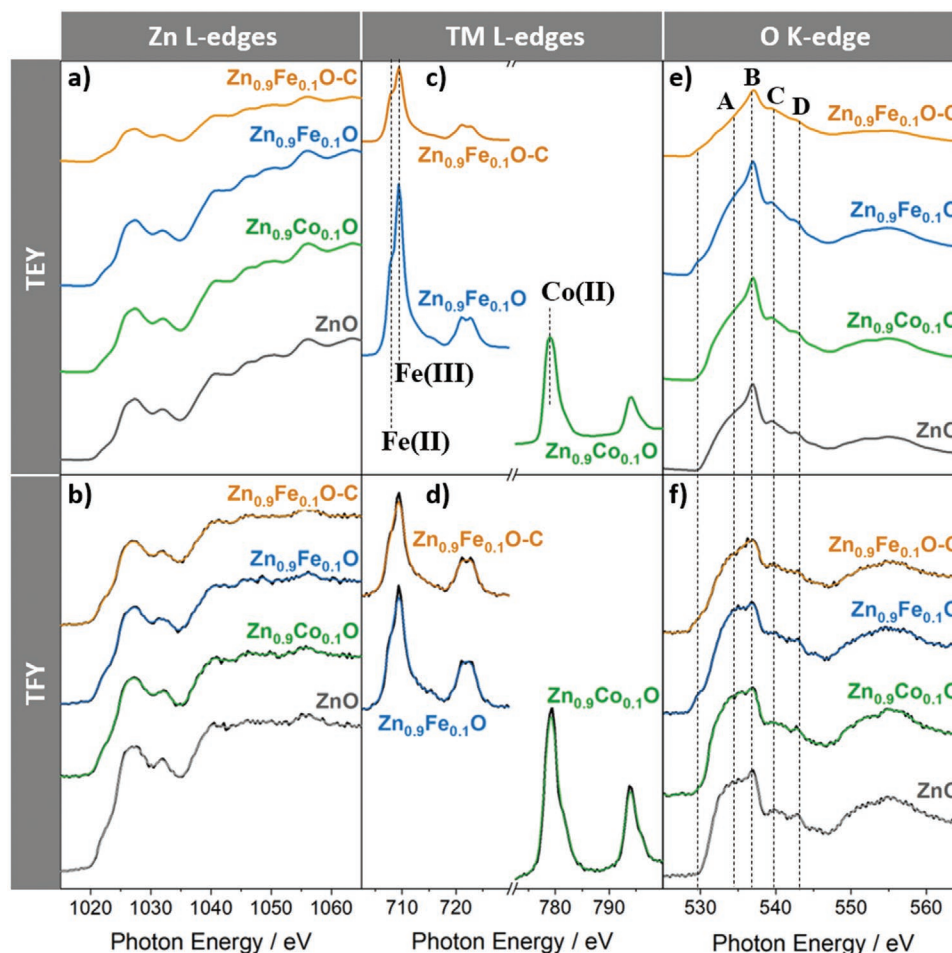
Figure 1. Soft XAS data of pristine electrodes based on ZnO (in black), $Zn_{0.9}Co_{0.1}O$ (in green), $Zn_{0.9}Fe_{0.1}O$ (in blue), and $Zn_{0.9}Fe_{0.1}O–C$ (in orange) as active material: a) TEY and b) TFY spectra at the Zn L-edges; c) TEY and d) TFY spectra at the TM L-edges; e) TEY and f) TFY spectra at the O K-edge. The same general color code is also used in the following figures; all spectra were shifted vertically for the sake of clarity.

of metallic zinc and lithium. The delithiation profile shows that the dealloying reaction follows several distinct voltage steps, which are absent for TM-doped ZnO – presumably due to the substantially larger size of the $Zn^0/LiZn$ nanograins.[28,37] At the same time, the reversible capacity obtained at elevated potentials is substantially lower for pure ZnO compared to the TM-doped samples, which has been assigned to the beneficial effect of the TM doping, favoring the reconversion of Li_2O due to the formation of percolating TM nano-network upon lithiation and the suppression of the $Zn^0/LiZn$ nanograin growth.[26,28,37] $Zn_{0.9}Co_{0.1}O$ features a very similar shape for the lithiation reaction as ZnO; just with a slightly higher voltage for the extended potential plateau related to the conversion reaction as a result of the cobalt doping.[28] The curve of Fe-doped ZnO, however, includes two rather long (slightly sloped) potential plateaus upon lithiation. The first one at around 0.75 V has been assigned earlier to an initial Li^+ insertion into cationic vacancies resulting from the aliovalent Fe^{3+} doping, followed by a kinetically favored conversion reaction.[30,32] The alloying reaction contribution is generally comparable for all samples; a little lower for the TM-doped samples due to the relatively lower Zn content. The overall delithiation capacity, however,

is substantially larger for the TM-doped samples. This is due to the better reversibility of the conversion reaction, being the highest for $Zn_{0.9}Co_{0.1}O$ and $Zn_{0.9}Fe_{0.1}O$ and only slightly lower for $Zn_{0.9}Fe_{0.1}O–C$, as the carbon coating has been included in the calculation of the specific capacity. Figure 2b compares the cycling stability, revealing that $Zn_{0.9}Co_{0.1}O$ and $Zn_{0.9}Fe_{0.1}O–C$ provide very stable cycling, while the capacity of electrodes based on $Zn_{0.9}Fe_{0.1}O$ and ZnO fades continuously. ZnO shows the most severe capacity fading, leading to a specific capacity of around 300 mAh g^{-1} after 20 cycles, which is attributed to the increasing irreversible Li_2O formation. In contrast, Co-doped ZnO offers a very high initial capacity and very stable cycling with a high reversible specific capacity of 943 mAh g^{-1} after 20 cycles. Also, the introduction of Fe allows for a high initial capacity, but stable cycling can only be achieved after the application of the carbon coating. The latter results in slightly lower specific capacities compared to $Zn_{0.9}Co_{0.1}O$ because of the added coating weight. Based on this comparative electrochemical characterization, we chose the dis-/charge potential values as displayed in Figure 2c–f for the ex situ analysis via soft XAS to cover the main electrochemical features and distinct reaction steps, that is, one after each potential plateau upon lithiation

**ADVANCED
SCIENCE NEWS**

www.advancedsciencenews.com

**small
methods**

www.small-methods.com
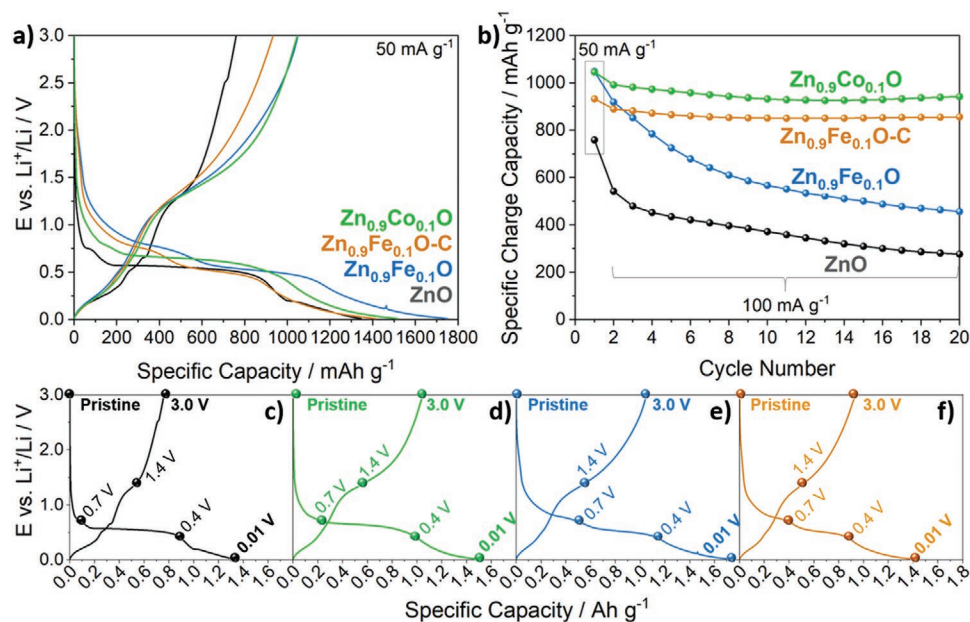
Figure 2. a) First cycle dis-/charge profiles for half-cells comprising ZnO, $Zn_{0.9}Co_{0.1}O$, $Zn_{0.9}Fe_{0.1}O$, and $Zn_{0.9}Fe_{0.1}O–C$ as the active material for the working electrode (first cycle: 0.05C). b) Cycling performance for 20 cycles of the same cells (subsequent cycles at 0.1C). c–f) First cycle dis-/charge profiles with the distinct potential values at which electrodes were collected for the ex situ XAS (all) and XPS (bold) analysis.

(0.7 and 0.4 V), in the fully lithiated state (0.01 V), after the dealloying reaction (1.4 V), in the fully delithiated state (3.0 V), and after 20 cycles (fully delithiated). For the ex situ XPS analysis, we restricted the number of samples to the fully lithiated state, the fully delithiated state, and after 20 cycles (fully delithiated). All samples declared as "20 cycles" within this study refer to fully delithiated electrodes recovered after 20 cycles.

2.4. Soft XAS and XPS Analysis – Cycled Electrodes

The SEI thickness was qualitatively estimated by a combination of XPS and XAS – the latter was performed in both TEY and TFY mode at the Zn L_3-edge (around 1020 eV). At this energy, these three techniques are complementary with respect to their surface sensitivity. The ID of XPS depends solely on the mean free path of the photoelectrons,[38] which is limited to a few nanometers at the sample surface at binding energies in the Zn 2p region and when using Al K_α radiation.[38] In the TEY mode (XAS), photoelectrons, Auger electrons, and secondary electrons contribute to the overall measured photocurrent,[39] which in the present case means that the ID is greater compared to XPS. The ID for the TEY measurements at the Zn L_3-edge has been estimated to be around 10 nm.[34] In the TFY mode (XAS), the emitted photons are detected, which leads to a substantially higher ID, in the range of 75 to 100 nm.[34,40] Accordingly, we assume the ID to be about 3, 10, and 75 nm in the case of XPS, TEY (XAS), and TFY (XAS), respectively. It should be noted, however, that it might be even greater, as the SEI is a porous film (covering the porous electrode) and it is composed of mostly light elements. Therefore, the following discussion remains rather qualitative and refers generally to inner and outer layers.

Figure 3a–d displays the Zn L_3-edge spectra collected in TEY mode. The pristine electrodes show fairly similar intensities, except for $Zn_{0.9}Fe_{0.1}O$-C in Figure 3d, which is assigned to the carbon coating. The spectra of $Zn_{0.9}Co_{0.1}O$ and $Zn_{0.9}Fe_{0.1}O–C$ after 20 cycles depict spectral features of re-oxidized Zn, while pure ZnO and $Zn_{0.9}Fe_{0.1}O$ show much less pronounced features of the zinc oxide, but rather oscillations related to metallic Zn^0. Those spectral differences are in good agreement with the electrochemical data, revealing substantially lower capacities after 20 cycles for electrodes containing the latter two materials (Figure 2b), and nicely demonstrate that the high specific capacities of $Zn_{0.9}Co_{0.1}O$ and $Zn_{0.9}Fe_{0.1}O–C$ are due to the very reversible conversion reaction. Furthermore, the comparison of the Zn L_3-edge intensities in the fully delithiated and fully lithiated states demonstrates that the four materials exhibit quasi-reversible SEI formation. The spectra collected in TFY mode are shown in Figure 3e–h and confirm the observations from the TEY experiments, that is, a higher degree of re-oxidized Zn in the case of $Zn_{0.9}Co_{0.1}O$ and $Zn_{0.9}Fe_{0.1}O–C$ compared to pure ZnO and $Zn_{0.9}Fe_{0.1}O$ (Figure 3f,g).

For a more detailed analysis, the Zn L_3-edge jumps were determined as the intensity difference before and after the L_3 edge, that is, at 1018 and 1035 eV, as a function of the state of charge. The values for the pristine electrodes were normalized to 100% and the relative intensity retention was determined for the different states of lithiation and delithiation (**Figure 4**). The results obtained in TEY mode for the Zn L_3-edge are summarized in Figure 4a. As indicated by the increase of Zn L_3 edge intensity upon delithiation, all four materials show quasi-reversibly formed SEI components, which are most pronounced for ZnO. In fact, Figure S6, Supporting Information, shows that a significant amount of Zn is detectable even by ex situ XPS when fully delithiated. This might be related to the

**ADVANCED
SCIENCE NEWS**
www.advancedsciencenews.com

**small
methods**
www.small-methods.com
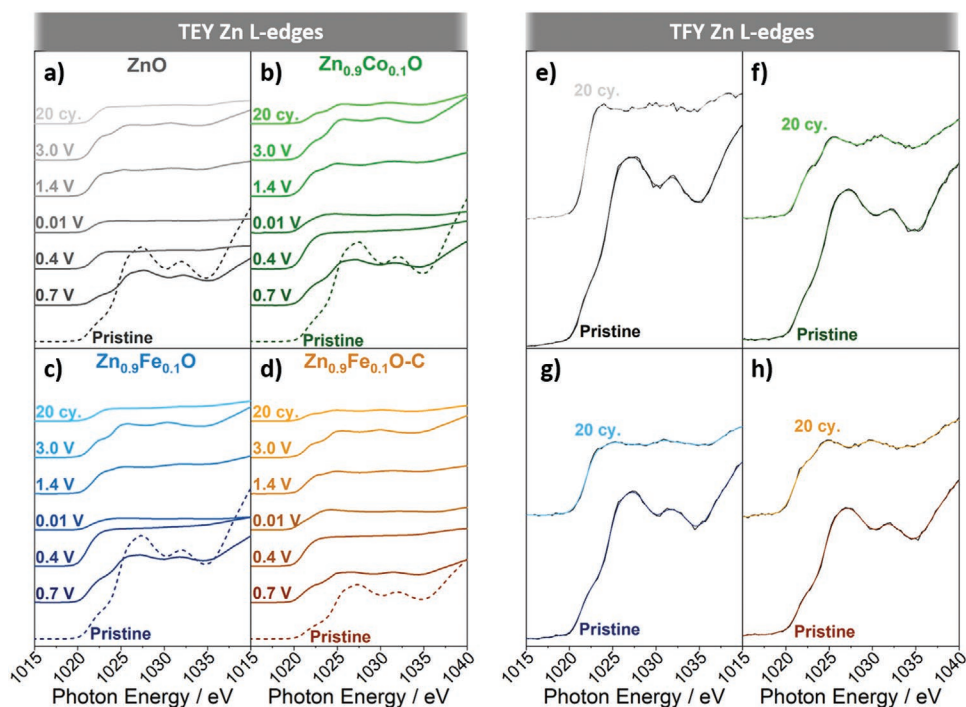
Figure 3. a–d) Zn L_3-edge XAS spectra of the electrodes based on a) ZnO, b) $Zn_{0.9}Co_{0.1}O$, c) $Zn_{0.9}Fe_{0.1}O$, and d) $Zn_{0.9}Fe_{0.1}O$-C as active material. e–h) Comparison of the Zn L_3-edge spectra recorded in total fluorescence mode (TFY) for the pristine electrodes and fully delithiated electrodes after 20 cycles for e) ZnO, f) $Zn_{0.9}Co_{0.1}O$, g) $Zn_{0.9}Fe_{0.1}O$, and h) $Zn_{0.9}Fe_{0.1}O$–C. The spectra were shifted vertically for the sake of clarity.

formation (and exposure) of relatively large metallic, that is, electronically conductive, Zn and LiZn nanograins upon lithiation, which are not re-oxidized upon delithiation[28,37] thus providing a sufficient electron supply for the oxidation of the

SEI (or specific SEI components). Interestingly, $Zn_{0.9}Fe_{0.1}O$-C shows a substantially thinner SEI when fully lithiated in the first cycle as compared to the other materials – or in other words, the retention remains the highest – most likely due to
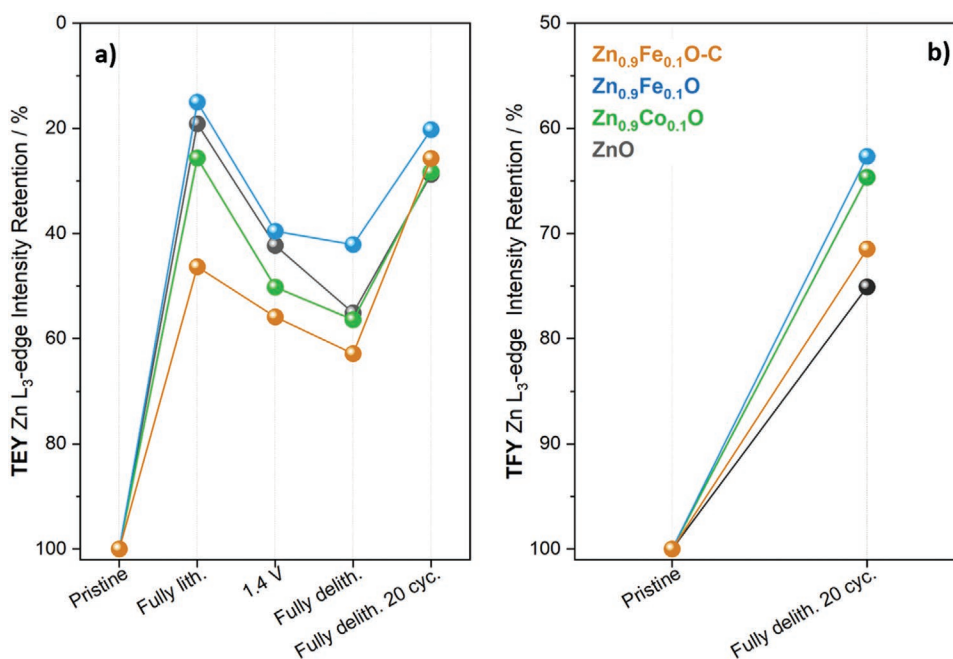
Figure 4. a) Zn L_3-edge intensity retention upon lithiation and delithiation from spectra collected in TEY mode. b) Zn L_3-edge intensity retention after 20 cycles collected in TFY mode.

the carbon coating which allows for a stabilized interface with the electrolyte. Also, the quasi-reversible capacity contribution arising from the SEI is substantially lower upon delithiation compared to the other materials. These results are remarkable, since the uncoated Fe-doped ZnO reveals a thicker SEI or, accordingly, lower Zn L_3-edge intensities in general. Nevertheless, the SEI thickens over the consecutive 20 cycles for all four samples and eventually reaches a comparable thickness on the basis of the TEY results. It should be kept in mind, though, that the intensity decays exponentially with an increasing SEI film thickness and the L_3-edge intensities are rather low for electrodes recovered in the fully delithiated state after 20 cycles. Accordingly, the values obtained in TEY mode are less comparable after 20 cycles. Hence, we performed the same analysis in TFY mode, comparing the pristine electrodes with those subjected to 20 cycles. The results, displayed in Figure 4b, illustrate the intensity retention of the Zn L_3-edge TFY spectra. The data clearly indicate that the SEI grows thicker when ZnO is doped with iron or cobalt compared to pure ZnO and that this effect is reduced by the carbon coating. The fact that the Zn L_3-edges in TEY do not fully vanish in combination with the relatively moderate intensity decay in the TFY spectra suggests that the SEI for all materials does not grow thicker than ≈25–35 nm.

### 2.4.1. Composition of the SEI – Carbonates, Oxides, and Organic Components

Figure S7a, Supporting Information, shows the carbon K-edge soft XAS spectra recorded for the pristine electrodes. All spectra exhibit the same spectral features and intensities and, thus, provide a good basis for the comparison of any changes induced by the electrochemical de-/lithiation in the ex situ analysis. The spectra of all materials are dominated by the spectral features of graphitic carbon from the conductive agent at 285.2 eV and ≈292.0 eV, arising from 1s–π^* and 1s–σ^* transitions, respectively.[41] This includes also the spectrum of $Zn_{0.9}Fe_{0.1}O$–C, which does not show a major contribution arising from the carbon coating, even though the carbon coating itself contains different carbon species, as apparent from the comparison of the pristine $Zn_{0.9}Fe_{0.1}O$-C electrode and the simple powder (Figure S7b, Supporting Information).

The X-ray photoelectron spectra for the C 1s region of the cycled electrodes are displayed in **Figure 5**a–d. The main signal at 285.0 eV is assigned to C−C and hydrocarbon species. The peak at 286.5 eV is typically assigned to C−O species.[42] The peaks at 288.9 and 290.3 eV arise from alkyl carbonates ($ROCO_2Li$) and Li_2CO_3, respectively, originating from the reduction of the organic carbonate solvent, especially EC.[43,44] Overall, the spectra are comparable for all four materials, revealing a similar composition. Given that the peaks with the highest intensity are related to the presence of C−C/hydrocarbons and C−O species, independent of the state of charge, indicates that the outer layer of the SEI is mostly composed of aliphatic carbon and organic C−O components. Interestingly, though, the peak for lithiated carbon at around 283.0 eV shows the highest intensity at 3.0 V (compared to 0.01 V and after 20 cycles). This is in line with the abovementioned quasi-reversible SEI formation, while simultaneously indicating

that the lithiation of the conductive carbon is at least not fully reversible and some lithium remains trapped inside.

The X-ray photoelectron spectra of the oxygen 1s region are depicted in Figure 5e–h. In the fully lithiated state (0.01 V), all samples show a large peak, assigned to the convolution of lithium carbonate and alkyl carbonates.[45,46] The peak at 528.0 eV can be assigned to Li_2O in the SEI. The peak at a binding energy of 533.6 eV is typically assigned to oxygen in C−O bonds. However, these bonds are present in the sodium carboxymethyl cellulose (Na-CMC) binder as well, which provides an explanation for the observation that the intensity does not change during cycling.[46] Furthermore, all spectra show a feature at 530.7 eV, which can be assigned to lithium alkoxides (ROLi).[43] A potential contribution from ZnO, which would appear in the same range, can be ruled out due to the low Zn $2p_{3/2}$ intensities throughout the lithiated and delithiated states (compare Figure S6, Supporting Information). The ROLi feature at 530.7 eV becomes less intense when the electrodes are subsequently delithiated (3.0 V), indicating that this component is formed quasi-reversibly – or in other words re-oxidized. In the case of pure ZnO, this quasi-reversibility appears to be the highest, which is in good agreement with the observation that ZnO shows the highest contribution of a quasi-reversible SEI formation (see Figure 4a).

Figure 6a–d shows the carbon K-edge spectra collected in TEY mode. Generally, the comparison of the evolution of the spectra recorded for each sample shows a very similar trend in all cases. More specifically, the spectral features A_1-C_2 (see below) appear for all samples (highlighted by dashed lines). All components of the final SEI are present already at 0.7 V, that is, there are no additional features appearing upon further lithiation (and subsequent delithiation), which is in line with the electrochemical stability of the electrolyte toward reduction, which is limited to about 0.8 V.[3,47] Overall, the intensity of the spectra decreases upon lithiation and increases upon delithiation, which is reflected by the decreasing and increasing, respectively, underlying signal of the conductive carbon. For instance, there is a substantial decrease and increase in the intensity of the A_1 feature at ≈285.0 eV, which is related to the 1s–π^* transition of graphitic carbon. The same holds true for the A_2 feature at ≈292.0 eV, which is related to the 1s–σ^* transition of graphitic carbon (see also Figure S7a, Supporting Information). Different from the other features, however, the A_1 peak remains rather pronounced throughout cycling, which is assigned to the fact that lithiated graphitic carbon[48] and Li_2CO_3[49] also show a feature in this region. In fact, Li_2CO_3 is the major component in all spectra with a large peak C_1 at ≈290.4 eV related to the C=O 1s–π^* transition and the two peaks of feature C_2 at around 297.5 and 301.0 eV related to the C−O and C=O 1s–σ^* resonances. The peak at around 290.4 eV, however, is not solely due to Li_2CO_3, since also lithiated carbon exhibits a dominant spectral feature in that range.[48] Feature B at around 288.5 eV is typically assigned to either the C−O 1s–π^* transition or the 1s–σ^* transition, occurring for the σ-bonds of both C−C and −CH$_2$.[41] Rezvani et al.[24,25] have shown that this feature can be directly correlated with $ROCO_2Li$, becoming the most intense SEI peak for the spinel-structured $ZnFe_2O_4$ in the fully lithiated state. Interestingly, this behavior is not observed for the (TM-doped) ZnO materials. One possible explanation is a potentially larger ID of the measurements presented herein as compared

ADVANCED
SCIENCE NEWS
www.advancedsciencenews.com

small
methods
www.small-methods.com
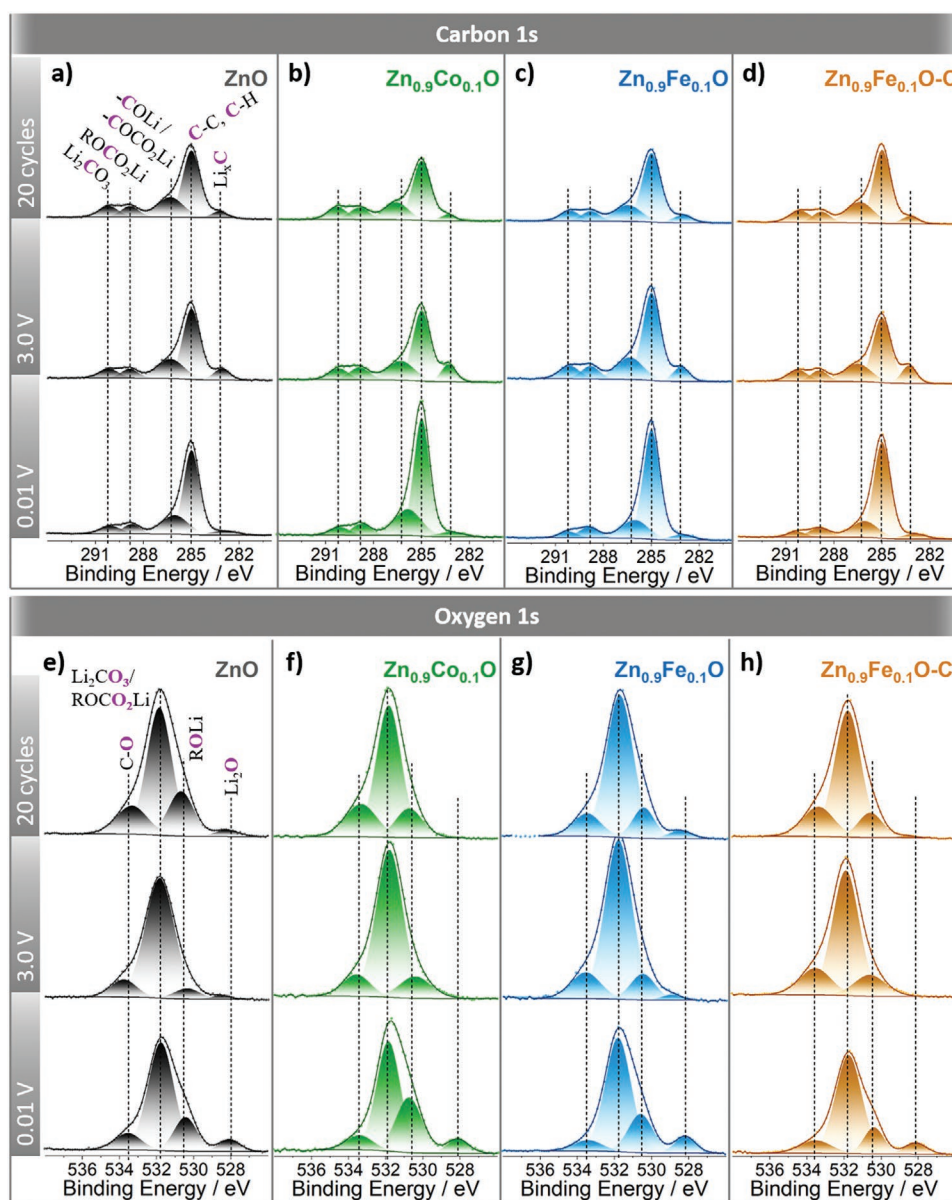
Figure 5. a–d) XPS spectra of the carbon 1s region for cycled electrodes based on a) pure ZnO, b) $Zn_{0.9}Co_{0.1}O$, c) $Zn_{0.9}Fe_{0.1}O$, and d) $Zn_{0.9}Fe_{0.1}O$-C as active material. For each material, the cycling was stopped either at 0.01 V in the initial lithiation, at 3.0 V after the first delithiation, and at 3.0 V after 20 cycles are presented. e–h) XPS spectra of the oxygen 1s region for e) pure ZnO, f) $Zn_{0.9}Co_{0.1}O$, g) $Zn_{0.9}Fe_{0.1}O$, and h) $Zn_{0.9}Fe_{0.1}O$–C at the same states of de-/lithiation as in (a–d).

to the study of Rezvani et. al.,[25] and/or a thinner $ROCO_2Li$ layer, leading to the coverage of the intensity changes of the $ROCO_2Li$ component by the much stronger Li_2CO_3 signal. Besides, one major difference recognized when comparing the materials with each other is that the intensities of the features B and C_1 in $Zn_{0.9}Fe_{0.1}O$ (Figure 6c) decrease upon cycling when comparing the fully lithiated state after one cycle (3.0 V) and 20 cycles, while for the other materials, the intensity of these features increases (Figure 6a,b,d). This difference becomes even more evident after background subtraction for the corresponding peaks and direct intensity comparison (Figure S8a–d, Supporting Information), indicating a decrease of the carbonate and organic species upon cycling for $Zn_{0.9}Fe_{0.1}O$.

In order to further elucidate this behavior, we take a closer look at the soft XAS spectra collected in the TEY mode at the oxygen K-edge, displayed in Figure 6e–h. All oxygen spectra depict generally increasing and decreasing intensities during lithiation and delithiation, respectively, in the first cycle, which is in good agreement with the thickness evaluation in Figure 4. This suggests that oxygen-containing species contribute to the quasi-reversible SEI formation. The features B_1 (at 533.4 eV) and B_2 (at around 540.0 and 544.0 eV) can be assigned to the C=O 1s–π^* transition and the C–O and C=O 1s–σ^* transition in Li_2CO_3.[50,51] Furthermore, all spectra also show a shoulder of peak A at around 532.2 eV, which is related to $ROCO_2Li$ alkyl carbonates.[25] Note that the latter signal also overlaps
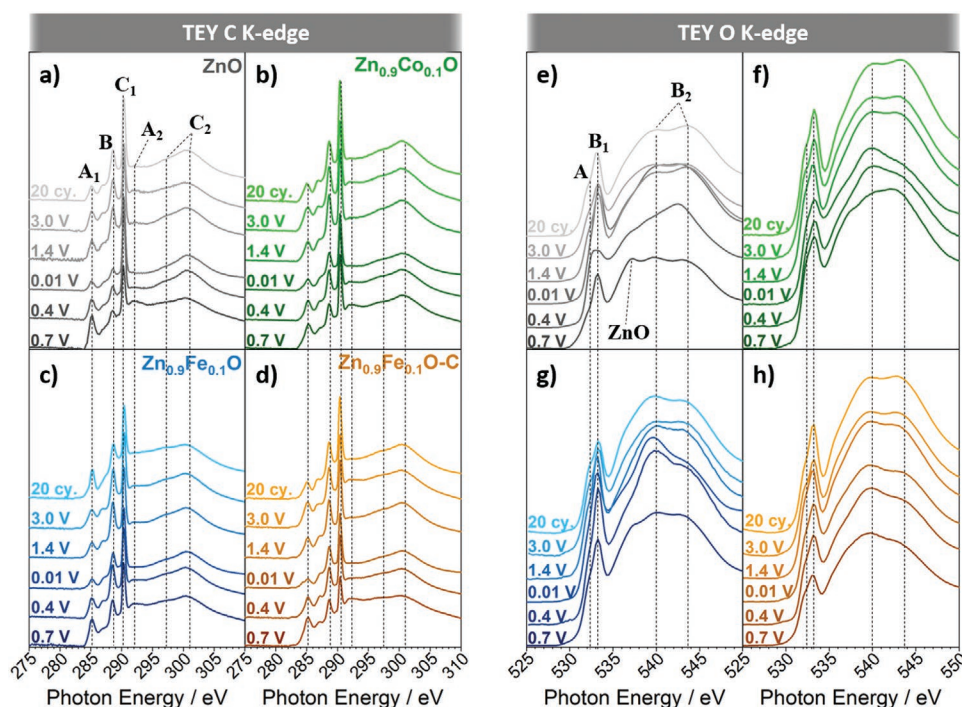
Figure 6. a–d) Carbon K-edge XAS spectra of the electrodes based on a) ZnO, b) $Zn_{0.9}Co_{0.1}O$, c) $Zn_{0.9}Fe_{0.1}O$, and d) $Zn_{0.9}Fe_{0.1}O–C$ as active material. e–h) Oxygen K-edge XAS spectra of the same electrodes based on e) ZnO, f) $Zn_{0.9}Co_{0.1}O$, g) $Zn_{0.9}Fe_{0.1}O$, and h) $Zn_{0.9}Fe_{0.1}O–C$. The spectra were shifted vertically and peak assignments are only shown in the panels for pure ZnO for the sake of clarity.

with a peak of Li_2O.[51,52] For ZnO, the shoulder peak A is most intense upon lithiation, for example, at 0.4 V and, thus, after the conversion reaction (Figure 6e). This increase in intensity of feature A is ascribed to the formation of larger Li_2O aggregates during the conversion reaction, since pure ZnO lacks the "confinement effect" by the transition metal nano-network.[17] In fact, also the lithium K-edge spectra show an increasing amount of Li_2O when reaching 0.4 V (Figure S9, Supporting Information).

Differently, $Zn_{0.9}Co_{0.1}O$ and $Zn_{0.9}Fe_{0.1}O$ (Figure 6f,g) do not show such behavior and the features B_1 and B_2 of Li_2CO_3 dominate the overall spectra at 0.4 V. When $Zn_{0.9}Co_{0.1}O$ and $Zn_{0.9}Fe_{0.1}O$ are fully lithiated, the intensity of the B_2 peak at lower photon energy (540.0 eV) is higher than that of the higher energy feature. This is opposite for pure ZnO. Since the spectral feature at around 540.0 eV is related to the C−O 1s–σ^* transition, this indicates a higher amount of ROLi (alkoxides) for the TM-doped samples.[50] The oxygen K-edge spectra of $Zn_{0.9}Fe_{0.1}O–C$ reveal a rather stable behavior with increasing and decreasing intensities upon lithiation and delithiation, respectively, which is in good agreement with the trend of the carbon XAS spectra.

Interestingly, after 20 cycles, the overall intensity of the oxygen spectra for pure ZnO, $Zn_{0.9}Co_{0.1}O$, and $Zn_{0.9}Fe_{0.1}O–C$ increases, while it (slightly) decreases for $Zn_{0.9}Fe_{0.1}O$ (see also Figure S8e–h, Supporting Information, for a direct comparison) – just like for the C K-edge spectra (Figure S8a–d, Supporting Information). A possible explanation for this difference is that the overall contribution of oxygen species, and specifically Li_2CO_3, in the SEI decreases upon cycling for $Zn_{0.9}Fe_{0.1}O$,

while other species become more dominant in the SEI. In fact, the oxygen fluorescence spectra (Figure S10, Supporting Information) with their larger ID show that the overall intensity of the spectra is substantially lower for $Zn_{0.9}Fe_{0.1}O$ than for the other materials after 20 cycles, indicating the average oxygen content in the extended surface region for this sample after cycling than for the other ones. Moreover, the oxygen K-edge spectra after 20 cycles in Figure S10, Supporting Information, are dominated by two rather broad peaks from Li_2O, suggesting increased amounts of the latter in the deeper layers of the SEI.

2.4.2. Composition of the SEI – Fluorine-Containing Species

The fluorine TEY K-edge spectra for all materials and lithiation states are depicted in **Figure 7**a–d. All samples show decreasing fluorine intensities upon lithiation and increasing intensities upon delithiation, indicating that fluorine containing species are mostly formed in the inner SEI layers, which is in good agreement with the findings for the SEI on graphite and lithium metal.[8] When comparing the different samples, though, the intensity in the fully lithiated state is generally lower for $Zn_{0.9}Co_{0.1}O$ and $Zn_{0.9}Fe_{0.1}O$ compared to ZnO and $Zn_{0.9}Fe_{0.1}O–C$. This is in line with the findings from the analysis of the O K-edge spectra, which revealed higher amounts of organic alkoxides in the outer layers of the SEI on $Zn_{0.9}Co_{0.1}O$ and $Zn_{0.9}Fe_{0.1}O$ (Figure 6e–h). Besides, the main spectral features in all spectra arise from LiF and P–F species. Those P–F species are most likely a combination of $LiPF_6$ salt residuals (despite the rinsing with dimethyl carbonate (DMC)) as well as
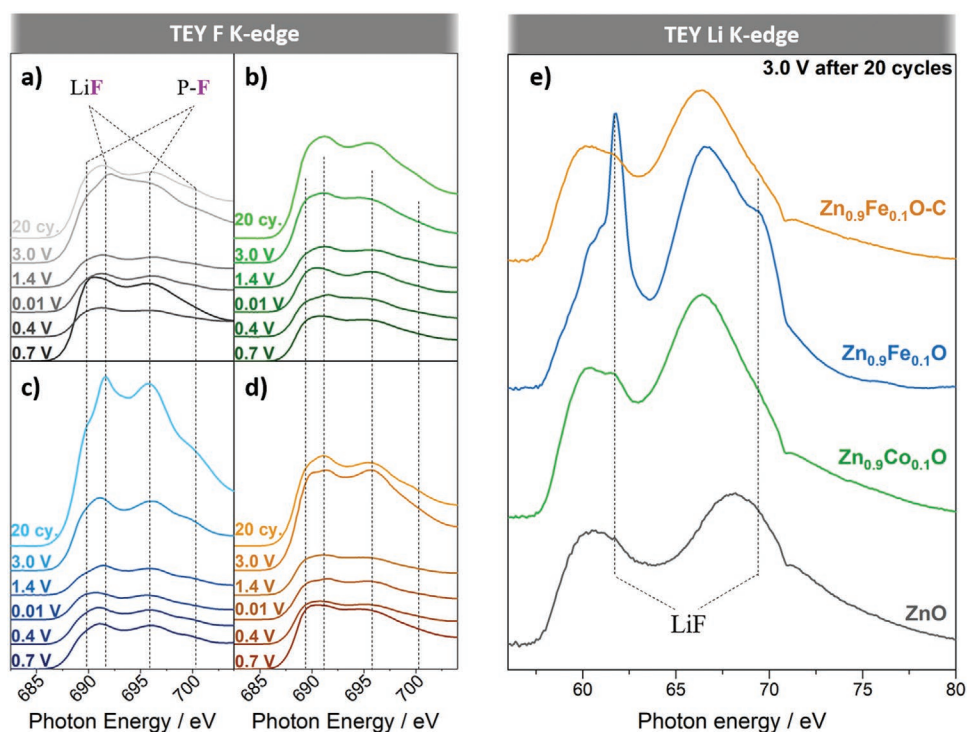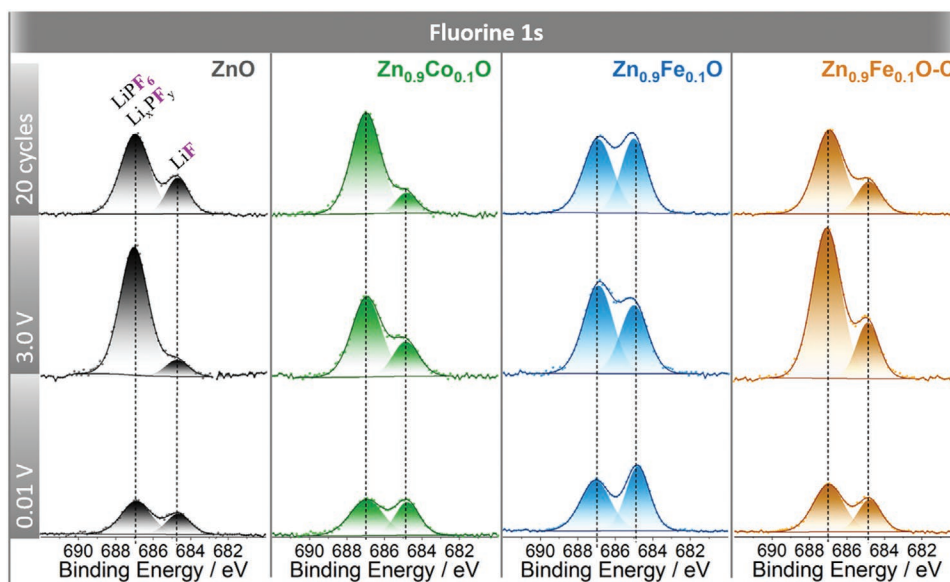
Figure 7. a–d) Fluorine K-edge XAS spectra of the electrodes based on a) ZnO, b) $Zn_{0.9}Co_{0.1}O$, c) $Zn_{0.9}Fe_{0.1}O$, and d) $Zn_{0.9}Fe_{0.1}O$–C as active material. e) Lithium K-edge XAS spectra of fully delithiated electrodes after 20 cycles. The spectra were shifted vertically for the sake of clarity.

Li_xPF_y salt decomposition products; the latter are presumably dominating.[53] Remarkably, when comparing the spectra for all materials after 20 cycles, we find that the intensity is slightly lower for ZnO (Figure 7a) and $Zn_{0.9}Fe_{0.1}O$–C (Figure 7d), which suggests a rather stable fluorine-containing inner SEI layer, which is subsequently covered by different, fluorine-poor or even fluorine-free SEI components. Differently, for $Zn_{0.9}Co_{0.1}O$ (Figure 7b), there is a slight increase upon cycling, indicating that additional salt decomposition occurs also upon continuous cycling. In the case of $Zn_{0.9}Fe_{0.1}O$, this is even more pronounced (Figure 7c), especially the increase of the LiF-related features.

This finding is further supported by the TEY Li K-edge spectra recorded after 20 cycles (Figure 7e). The spectra of ZnO, $Zn_{0.9}Co_{0.1}O$, and $Zn_{0.9}Fe_{0.1}O$-C show very similar features, dominated by the broad Li_2CO_3-related peaks at around 61.0 and 67.0 eV, with only small additional features for LiF in the spectrum of $Zn_{0.9}Co_{0.1}O$. On the contrary, the spectrum of $Zn_{0.9}Fe_{0.1}O$ shows a sharp peak at 61.8 eV and a very pronounced shoulder peak at about 70.0 eV, which can be clearly assigned to LiF.[34] As a matter of fact, while a certain fraction of LiF in the inner layer has been reported to be beneficial for a stable SEI,[43] such an extensive enrichment of LiF in the SEI has the opposite effect, negatively impacting the electrochemical performance.[54] In fact, electrochemical impedance spectroscopy (EIS) performed after an increasing number of cycles reveal that the impedance is significantly increasing in the case of $Zn_{0.9}Fe_{0.1}O$, while there is only a moderate increase in the case of $Zn_{0.9}Co_{0.1}O$ (Figure S11, Supporting Information). An ex situ SEM

analysis of the cycled electrodes (Figure S12, Supporting Information), moreover, suggests that there is slightly more SEI formed – in line with the soft XAS results and the electrochemical data. The corresponding EDX mapping further supports the trend regarding the fluorine concentration, that is, lower values for ZnO and $Zn_{0.9}Fe_{0.1}O$–C and the highest concentration for $Zn_{0.9}Fe_{0.1}O$ (Figure S13, Supporting Information). These findings, thus, provide an explanation for the inferior electrochemical performance of $Zn_{0.9}Fe_{0.1}O$ electrode compared to $Zn_{0.9}Co_{0.1}O$ and carbon-coated $Zn_{0.9}Fe_{0.1}O$–C (in addition to the greater electrolyte decomposition and SEI formation in general), indicating that iron doping specifically triggers the continuous electrolyte decomposition. This is also in good agreement with a thicker SEI on $Zn_{0.9}Fe_{0.1}O$, as shown in Figure 4b and TFY O K-edge spectra in Figure S10, Supporting Information.

To confirm this important finding, we conducted an XPS analysis of the fluorine 1s region (**Figure 8**). Generally, all spectra show two main contributions, LiF at ≈685 eV and P–F species at ≈687 eV,[45] which is in excellent agreement with the TEY F K-edge spectra (Figure 7a–d). Also, the general trend is in good agreement with the soft XAS results. In the fully lithiated state (0.01 V), the overall intensity is rather low, indicating the presence of other, fluorine-free species on top in the surface-near region of the SEI. In the fully delithiated state, the intensity is generally increasing, suggesting the quasi-reversible formation of some of the SEI components. Furthermore, the overall intensity decreases after 20 cycles for pure ZnO (Figure 8a) and $Zn_{0.9}Fe_{0.1}O$–C (Figure 8d) and (slightly) increases for $Zn_{0.9}Co_{0.1}O$ (Figure 8b) and $Zn_{0.9}Fe_{0.1}O$
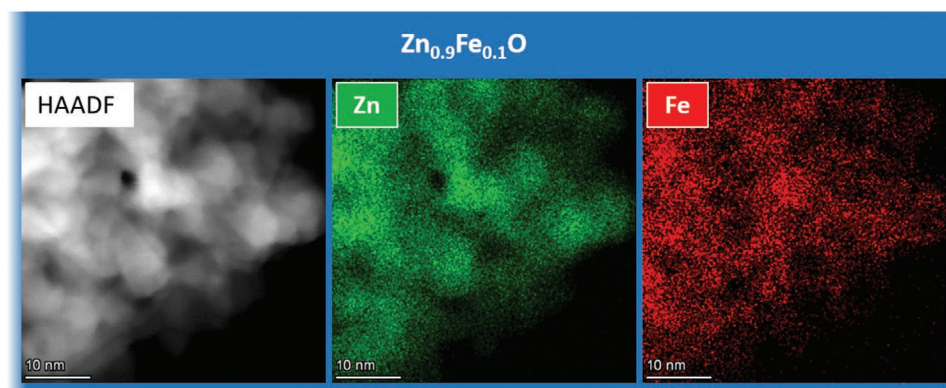
Figure 8. XPS spectra of the fluorine 1s region for cycled electrodes based on a) ZnO, b) $Zn_{0.9}Co_{0.1}O$, c) $Zn_{0.9}Fe_{0.1}O$, and d) $Zn_{0.9}Fe_{0.1}O$–C as active material. The cells were stopped in the fully lithiated state (0.01 V), the fully delithiated state (3.0 V), and after 20 cycles (in the fully delithiated state). All spectra have the same intensity scale.

(Figure 8c). Specifically, for $Zn_{0.9}Fe_{0.1}O$, there is a substantially larger fraction of LiF detected, which increases upon cycling, as observed also by soft XAS (Figure 7).

In order to rule out that the detrimental effect of the presence of iron at the interface with the electrolyte is related to an inhomogeneous distribution of Fe within the nanoparticles, we tested this by TEM imaging and EDX mapping. The results presented in **Figure 9** reveal a rather homogeneous Fe distribution without any apparent higher concentration at the near-surface region of the particle. Accordingly, the presence of iron at the surface might generally be avoided, for example, by applying a carbon coating or by realizing core-shell structures with an iron-containing particle core and a cobalt (or another suitable TM dopant) comprising shell. These findings also provide an explanation for the common observation that iron-based anode materials provide suitable cycling only after applying some carbon coating and/or embedding the iron-based active materials in carbonaceous matrices.[55–58]

3. Conclusion

The introduction of transition metal dopants into ZnO generally enhances the electrochemical performance and cycling stability. Nonetheless, a remarkable difference is observed between Fe and Co. While the latter results in very stable capacities, the incorporation of Fe leads to initially much higher capacities compared to ZnO, though followed by a faster fading than $Zn_{0.9}Co_{0.1}O$. The fact that this fading can be avoided by applying a carbon coating indicates that interfacial reactions with the electrolyte play a decisive role. Indeed, Fe doping is found to trigger electrolyte decomposition and, in particular, the formation of a large amount of LiF, which eventually has a detrimental impact on the capacity retention. Besides, all materials reveal a quasi-reversible SEI formation, mostly composed of oxygen-containing species, which is most pronounced for ZnO upon the first cycle and less pronounced for $Zn_{0.9}Fe_{0.1}O$–C, that is, upon application of the carbon coating. The latter also enables a stable inner fluorine-rich SEI layer, while the non-coated TM-doped

Figure 9. TEM-EDX mapping of $Zn_{0.9}Fe_{0.1}O$ for Zn (in green) and Fe (in red).

**ADVANCED
SCIENCE NEWS**

www.advancedsciencenews.com

**small
methods**

www.small-methods.com

samples provide a larger fraction of ROLi as SEI component and generally a thicker SEI after 20 cycles. Taken together, these findings highlight the great importance of carefully considering the elemental composition of potential next-generation anode materials, especially at the particle surface, in order to realize stable interphases at the electrode|electrolyte interface.

4. Experimental Section

Material Synthesis: $Zn_{0.9}TM_{0.1}O$ samples were synthesized following a previously reported procedure.[32] Stoichiometric amounts of zinc (II) gluconate (Alfa Aesar) and either cobalt (II) gluconate hydrate (ACROS ORGANICS) or iron (II) gluconate dihydrate (Sigma–Aldrich) were dissolved in ultra-pure water with a total ion concentration of 0.2 mol L^{-1}. The latter solution was slowly added to a second solution comprising 1.2M sucrose, and the obtained solution was stirred for 15 min. The water was evaporated under continuous stirring at 160 °C and, subsequently, the temperature was increased to 300 °C in order to initiate the sucrose decomposition. After cooling down, the precursor was ground and calcined in a muffle furnace (Nabertherm) for 3 h at 400 °C for $Zn_{0.9}Co_{0.1}O$ and 450 °C for ZnO and $Zn_{0.9}Fe_{0.1}O$ (heating rate of 3 °C min^{-1}). The carbon coating was formed by dispersing/dissolving $Zn_{0.9}Fe_{0.1}O$ and sucrose in ultrapure water in a weight ratio of 1:0.5:3.5. The mixture was homogenized in a planetary ball mill (Fritsch Vario-Planetary Mill Pulverisette 4) for 3 h at 400/−800 rpm (1.5 h in each direction). The resulting dispersion was dried overnight at 80 °C and, subsequently, manually ground to obtain the solid precursor. This powder was calcined at 500 °C for 4 h in a tubular furnace (Nabertherm) with a heating rate of 3 °C min^{-1} under a constant argon flow.

Basic Physicochemical Characterization: X-ray diffraction (XRD) patterns were collected using a Bruker D8 advance diffractometer with Cu K_α radiation ($\lambda = 1.5406$ Å) in a 2θ range from 20° to 80° and a step size of 0.03°. Scanning electron microscopy (SEM) was performed using a Zeiss Crossbeam 340 field-emission electron microscope equipped with Oxford Instruments X-MaxN EDX detector. For the ex situ SEM/EDX studies, the cells were disassembled in an argon-filled glove box and transferred to the SEM again using an airtight transport box. Transmission electron microscopy (TEM) and energy-dispersive X-ray spectroscopy (EDX) were conducted using a Thermofisher Talos 200X TEM instrument with a dedicated SuperX EDX detector working at 200 kV. Thermogravimetric analysis (TGA) was conducted using a NETZSCH TG 209 F1 Libra under oxygen atmosphere and with a heating rate of 3 K min^{-1} from room temperature to 600 °C.

Electrochemical Characterization: Electrodes were prepared by mixing 75 wt% of the active material with 20 wt% Super C65 (Imerys), and 5 wt% sodium carboxymethyl cellulose (Na-CMC; Dow-Wolff Cellulosics) in a 1.25 wt% aqueous solution. Slurries were homogenized in a planetary ball mill (Fritsch Vario-Planetary Mill Pulverisette 4) for 3 h at 400/−800 rpm using 12 mL zirconia jars and zirconia balls. The resulting mixtures were cast on a dendritic copper foil (Schlenk) using a laboratory-scale doctor blade (BYK Additive & Instruments) with a wet film thickness of 120 µm and a casting speed of 50 mm s^{-1}. The electrode sheets were dried at room temperature overnight, before 12 mm round disc electrodes were punched with a puncher (Hohsen). All electrodes were dried for 12 h in a vacuum glass oven (Büchi B585) at 120 °C prior to the test. The resulting electrodes had an active material mass loading of 1.5–1.7 mg cm^{-2} and an electrode coating thickness of around 18 µm. Cells were assembled in an argon-filled glove box with less than 0.1 ppm of water and oxygen. All specific capacities reported in this study refer to the mass of the active material, including the mass of the carbon coating in the case of $Zn_{0.9}Fe_{0.1}O–C$. The electrochemical tests were performed in three-electrode Swagelok-type T-cells comprising lithium metal (Honjo Metal Co.) as the counter and reference electrodes. Glass fiber discs (Whatman GF/D, 13 mm), used as separators, were drenched with the electrolyte (1M $LiPF_6$ in the 3:7 weight mixture of ethylene carbonate (EC) and diethyl carbonate (DEC)). In addition, a Celgard separator was introduced at the working electrode side to avoid glass fiber contamination of the electrode surface. Galvanostatic cycling was conducted using a battery cycler (Maccor 4). The dis-/charge rate of 1C corresponded to a specific current of 1000 mA g^{-1}.

The electrodes for the ex situ characterization were recovered from the galvanostatically cycled cells in an argon-filled glove box. All electrodes were carefully rinsed twice with 500 µL of DMC, and dried under vacuum prior to the further experiments. EIS was performed at 20 °C in a frequency range of 1 to 10 mHz (voltage amplitude: 10 mV) using a Biologic VMP-3 potentiostat/galvanostat. The intermediate galvanostatic cycling was conducted in a potential range from 0.01 to 3.0 V at 0.05C for the first and 0.1C for the consecutive cycles.

Ex situ X-ray Photoelectron Spectroscopy (XPS): XPS measurements were performed in a PHI 5800 MultiTechnique ESCA system with monochromatized Al K_α radiation (1486.6 eV). The detection angle of the measurements was 45° and pass energies of 93.9 and 29.35 eV were used for the survey and detailed spectra, respectively. The samples were neutralized with electrons from a flood gun (current ≈3 µA) to compensate for charging effects at the surface. The binding energies of all spectra were calibrated to the C1s signal at 285 eV, which resulted in the F1s peak of LiF to be very close to 685 eV, and the data were analyzed using the CasaXPS software.

Ex situ Soft X-ray Absorption Spectroscopy (XAS): Soft XAS experiments were carried out using the radiation at the exit of the 8.1 bending magnet at the BEAR end-station BL8.1L (ELETTRA synchrotron facility, Trieste, Italy).[59] The spectral energy was calibrated by referring to the C 1s–π^* transitions (285.2 eV). The incident light was linearly polarized, and the incidence angle of the light with respect to the sample surface plane was kept fixed at 45° with the "S" polarization. The beam dimension was around 100 × 400 µm with an energy resolution between 0.1 and 0.2 eV. Samples were brought to the synchrotron in triple sealed vials under argon atmosphere. All electrodes were placed on the sample holder at the beamline in a glove bag kept under argon overpressure to avoid any contamination through ambient atmosphere. The samples were transferred to the XAS experimental chamber via an argon filled load-lock chamber. XAS measurements were performed in total electron yield (TEY) for all elements and total florescence yield (TFY) for selected elements, normalized to the incident photon flux.

Supporting Information

Supporting Information is available from the Wiley Online Library or from the author.

Acknowledgements

Conflict of Interest

The authors declare no conflict of interest.

Data Availability

The datasets generated during and/or analysed during the current study are available from the corresponding author on reasonable request.

[1] J. M. Tarascon, J. M. Tarascon, M. Armand, M. Armand, *Nature* **2001**, *414*, 359.

[2] D. Bresser, K. Hosoi, D. Howell, H. Li, H. Zeisel, K. Amine, S. Passerini, *J. Power Sources* **2018**, *382*, 176.

[3] K. Xu, *Chem. Rev.* **2004**, *104*, 4303.

[4] J. Asenbauer, T. Eisenmann, M. Kuenzel, A. Kazzazi, Z. Chen, D. Bresser, *Sustainable Energy Fuels* **2020**, *4*, 5387.

[5] J. Vetter, P. Novák, M. R. Wagner, C. Veit, K. C. Möller, J. O. Besenhard, M. Winter, M. Wohlfahrt-Mehrens, C. Vogler, A. Hammouche, *J. Power Sources* **2005**, *147*, 269.

[6] K. Edström, M. Herstedt, D. P. Abraham, *J. Power Sources* **2006**, *153*, 380.

[7] S. J. An, J. Li, C. Daniel, D. Mohanty, S. Nagpure, D. L. Wood, *Carbon N. Y.* **2016**, *105*, 52.

[8] E. Peled, S. Menkin, *J. Electrochem. Soc.* **2017**, *164*, A1703.

[9] W. J. Zhang, *J. Power Sources* **2011**, *196*, 13.

[10] M. N. Obrovac, V. L. Chevrier, *Chem. Rev.* **2014**, *114*, 11444.

[11] N. Nitta, G. Yushin, *Part. Part. Syst. Charact.* **2014**, *31*, 317.

[12] D. Liu, D. jiao Liu, X. Li, W. Xie, Q. Wang, Q. Liu, Y. Fu, D. He, *Small* **2017**, *13*, 1.

[13] C. Liang, M. Gao, H. Pan, Y. Liu, M. Yan, *J. Alloys Compd.* **2013**, *575*, 246.

[14] R. A. Huggins, *J. Power Sources* **1999**, *81–82*, 13.

[15] J. Cabana, L. Monconduit, D. Larcher, M. R. Palacín, *Adv. Mater.* **2010**, *22*, E170.

[16] M. D. Bhatt, J. Y. Lee, *Int. J. Hydrogen Energy* **2019**, *44*, 10852.

[17] D. Bresser, S. Passerini, B. Scrosati, *Energy Environ. Sci.* **2016**, *9*, 3348.

[18] J. Bai, X. Li, G. Liu, Y. Qian, S. Xiong, *Adv. Funct. Mater.* **2014**, *24*, 3012.

[19] D. Bresser, E. Paillard, R. Kloepsch, S. Krueger, M. Fiedler, R. Schmitz, D. Baither, M. Winter, S. Passerini, *Adv. Energy Mater.* **2013**, *3*, 513.

[20] Z. Zhao, G. Tian, A. Sarapulova, G. Melinte, J. L. Gómez-Urbano, C. Li, S. Liu, E. Welter, M. Etter, S. Dsoke, *ACS Appl. Mater. Interfaces* **2019**, *11*, 29888.

[21] A. Ponrouch, P. L. Taberna, P. Simon, M. R. Palacín, *Electrochim. Acta* **2012**, *61*, 13.

[22] S. Laruelle, S. Grugeon, P. Poizot, M. Dollé, L. Dupont, J.-M. Tarascon, *J. Electrochem. Soc.* **2002**, *149*, A627.

[23] L. Dupont, S. Laruelle, S. Grugeon, C. Dickinson, W. Zhou, J. M. Tarascon, *J. Power Sources* **2008**, *175*, 502.

[24] S. J. Rezvani, R. Gunnella, A. Witkowska, F. Mueller, M. Pasqualini, F. Nobili, S. Passerini, A. Di Cicco, *ACS Appl. Mater. Interfaces* **2017**, *9*, 4570.

[25] S. J. Rezvani, F. Nobili, R. Gunnella, M. Ali, R. Tossici, S. Passerini, A. Di Cicco, *J. Phys. Chem. C* **2017**, *121*, 26379.

[26] D. Bresser, F. Mueller, M. Fiedler, S. Krueger, R. Kloepsch, D. Baither, M. Winter, E. Paillard, S. Passerini, *Chem. Mater.* **2013**, *25*, 4977.

[27] J. Asenbauer, A. Varzi, S. Passerini, D. Bresser, *J. Power Sources* **2020**, *473*, 228583.

[28] F. Mueller, D. Geiger, U. Kaiser, S. Passerini, D. Bresser, *ChemElectroChem* **2016**, *3*, 1311.

[29] B. Liu, J. Zhang, X. Wang, G. Chen, D. Chen, C. Zhou, G. Shen, *Nano Lett.* **2012**, *12*, 3005.

[30] G. Giuli, T. Eisenmann, D. Bresser, A. Trapananti, J. Asenbauer, F. Mueller, S. Passerini, *Materials* **2017**, *11*, 49.

[31] J. Asenbauer, A. Hoefling, S. Indris, J. Tübke, S. Passerini, D. Bresser, *ACS Appl. Mater. Interfaces* **2020**, *12*, 8206.

[32] F. Mueller, A. Gutsche, H. Nirschl, D. Geiger, U. Kaiser, D. Bresser, S. Passerini, *J. Electrochem. Soc.* **2017**, *164*, A6123.

[33] G. Giuli, A. Trapananti, F. Mueller, D. Bresser, F. Dácapito, S. Passerini, *Inorg. Chem.* **2015**, *54*, 9393.

[34] A. Di Cicco, A. Giglia, R. Gunnella, S. L. Koch, F. Mueller, F. Nobili, M. Pasqualini, S. Passerini, R. Tossici, A. Witkowska, *Adv. Energy Mater.* **2015**, *5*, 1500642.

[35] S. J. Rezvani, Y. Mijiti, R. Gunnella, F. Nobili, A. Trapananti, M. Minicucci, M. Ciambezi, D. Bresser, S. Nannarone, S. Passerini, A. Di Cicco, *J. Phys. Chem. Solids* **2020**, *136*, 109172.

[36] S. Chen, N. V. Medhekar, J. Garitaonandia, K. Suzuki, *J. Phys. Chem. C* **2012**, *116*, 8541.

[37] C. J. Pelliccione, Y. Ding, E. V. Timofeeva, C. U. Segre, *J. Electrochem. Soc.* **2015**, *162*, A1935.

[38] A. Jablonski, C. J. Powell, *J. Vac. Sci. Technol., A* **2003**, *21*, 274.

[39] B. H. Frazer, B. Gilbert, B. R. Sonderegger, G. De Stasio, *Surf. Sci.* **2003**, *537*, 161.

[40] M. Kasrai, W. N. Lennard, R. W. Brunner, G. M. Bancroft, J. A. Bardwell, K. H. Tan, *Appl. Surf. Sci.* **1996**, *99*, 303.

[41] A. Augustsson, M. Herstedt, J. H. Guo, K. Edström, G. V. Zhuang, P. N. Ross, J. E. Rubensson, J. Nordgren, *Phys. Chem. Chem. Phys.* **2004**, *6*, 4185.

[42] S. Zhang, H. Du, J. He, C. Huang, H. Liu, G. Cui, Y. Li, *ACS Appl. Mater. Interfaces* **2016**, *8*, 8467.

[43] S. Malmgren, K. Ciosek, M. Hahlin, T. Gustafsson, M. Gorgoi, H. Rensmo, K. Edström, *Electrochim. Acta* **2013**, *97*, 23.

[44] L. Cabo-Fernandez, D. Bresser, F. Braga, S. Passerini, L. J. Hardwick, *Batteries Supercaps* **2019**, *2*, 168.

[45] V. Sharova, A. Moretti, T. Diemant, A. Varzi, R. J. Behm, S. Passerini, *J. Power Sources* **2018**, *375*, 43.

[46] S. J. Rezvani, M. Pasqualini, A. Witkowska, R. Gunnella, A. Birrozzi, M. Minicucci, H. Rajantie, M. Copley, F. Nobili, A. Di Cicco, *Appl. Surf. Sci.* **2018**, *435*, 1029.

[47] J. Kalhoff, G. G. Eshetu, D. Bresser, S. Passerini, *ChemSusChem* **2015**, *8*, 2154.

[48] L. Zhang, X. Li, A. Augustsson, C. M. Lee, J. E. Rubensson, J. Nordgren, P. N. Ross, J. H. Guo, *Appl. Phys. Lett.* **2017**, *110*, 104106.

[49] C. Yogi, D. Takamatsu, K. Yamanaka, H. Arai, Y. Uchimoto, K. Kojima, I. Watanabe, T. Ohta, Z. Ogumi, *J. Power Sources* **2014**, *248*, 994.

[50] D. A. Outka, J. Stöhr, R. J. Madix, H. H. Rotermund, B. Hermsmeier, J. Solomon, *Surf. Sci.* **1987**, *185*, 53.

[51] F. Frati, M. O. J. Y. Hunault, F. M. F. De Groot, *Chem. Rev.* **2020**, *120*, 4056.

[52] R. Qiao, Y. De Chuang, S. Yan, W. Yang, *PLoS One* **2012**, *7*, 3.

[53] G. G. Eshetu, T. Diemant, S. Grugeon, R. J. Behm, S. Laruelle, M. Armand, S. Passerini, *ACS Appl. Mater. Interfaces* **2016**, *8*, 16087.

[54] I. A. Shkrob, J. F. Wishart, D. P. Abraham, *J. Phys. Chem. C* **2015**, *119*, 14954.

[55] H. Xia, Y. Wan, G. Yuan, Y. Fu, X. Wang, *J. Power Sources* **2013**, *241*, 486.

[56] Y. Chen, H. Xia, L. Lu, J. Xue, *J. Mater. Chem.* **2012**, *22*, 5006.

[57] C. Lei, F. Han, D. Li, W. C. Li, Q. Sun, X. Q. Zhang, A. H. Lu, *Nanoscale* **2013**, *5*, 1168.

[58] X. Zhu, Y. Zhu, S. Murali, M. D. Stoller, R. S. Ruoff, *ACS Nano* **2011**, *5*, 3333.

[59] M. Pedio, G. Selvaggi, G. Naletto, M. G. Pelizzo, G. Tondello, *AIP Conf. Proc.* **2004**, *705*, 450.